Contents lists available at ScienceDirect

Pharmacological Research

Gut *Clostridium sporogenes*-derived indole propionic acid suppresses osteoclast formation by activating pregnane X receptor

Renpeng Peng [a,1], Chao Song [a,1], Shuangquan Gou [b,1], Haiyang Liu [a], Honglei Kang [a], Yimin Dong [a], Yong Xu [a], Peixuan Hu [a], Kaiyong Cai [b], Qian Feng [b,*], Hanfeng Guan [a,*], Feng Li [a,*]

[a] *Department of Orthopedic Surgery, Tongji Hospital, Tongji Medical College, Huazhong University of Science and Technology, Wuhan, China*
[b] *Key Laboratory of Biorheological Science and Technology, Ministry of Education, College of Bioengineering, Chongqing University, Chongqing, China*

ARTICLE INFO

ABSTRACT

Bone homeostasis is maintained by osteoclast-mediated bone resorption and osteoblast-mediated bone formation. A dramatic decrease in estrogen levels in postmenopausal women leads to osteoclast overactivation, impaired bone homeostasis, and subsequent bone loss. Changes in the gut microbiome affect bone mineral density. However, the role of the gut microbiome in estrogen deficiency-induced bone loss and its underlying mechanism remain unknown. In this study, we found that the abundance of *Clostridium sporogenes* (*C. spor.*) and its derived metabolite, indole propionic acid (IPA), were decreased in ovariectomized (OVX) mice. *In vitro* assays suggested that IPA suppressed osteoclast differentiation and function. At the molecular level, IPA suppressed receptor activator of nuclear factor kappa-B ligand (RANKL)-induced pregnane X receptor (PXR) ubiquitination and degradation, leading to increased binding of remaining PXR with P65. *In vivo* daily IPA administration or repeated *C. spor.* colonization protected against OVX-induced bone loss. To protect live bacteria from the harsh gastric environment and delay the emptying of orally administered *C. spor.* from the intestine, a *C. spor.*-encapsulated silk fibroin (SF) hydrogel system was developed, which achieved bone protection in OVX mice comparable to that achieved with repeated germ transplantation or daily IPA administration. Overall, we found that gut *C. spor.*-derived IPA was involved in estrogen deficiency-induced osteoclast overactivation by regulating the PXR/P65 complex. The *C. spor.*-encapsulated SF hydrogel system is a promising tool for combating postmenopausal osteoporosis without the disadvantages of repeated germ transplantation.

1. Introduction

The balance between osteoclast-mediated bone resorption and formation is critical for maintaining bone homeostasis. Excessive bone resorption is involved in pathological bone loss in diseases such as postmenopausal osteoporosis, Paget's bone disease, and periprosthetic osteolysis. Osteoclasts are derived from monocyte/macrophage lineage cells under the stimulation of two major cytokines—macrophage colony-stimulating factor (M-CSF) and receptor activator of nuclear factor kappa-B ligand (RANKL). M-CSF activates c-Fms to promote the proliferation and differentiation of monocytes into macrophages. RANKL binds to receptor activator of nuclear factor kappa-B (RANK) on the cell surface, and tumor necrosis factor receptor-associated factor 6 (TRAF6) is subsequently recruited to the inner cellular domain of RANK. p62 binds to TRAF6 and interacts with atypical protein kinase C (PKC),

followed by IκB kinase (IKK) complex activation [1]. Alternatively, TRAF6 forms a complex with transforming growth factor-β-activated kinase 1 (TAK1), which phosphorylates the IKK complex [2]. This complex subsequently phosphorylates IκB, leading to its proteasome-mediated degradation and nuclear translocation of free P65/RelA and p50 to the nucleus, resulting in the activation of master transcription factors essential for osteoclast differentiation [3]. RelA/P65 has been identified to inhibit c-Jun N-terminal kinase (JNK)-mediated apoptosis, and the absence of RelA/P65 results in a deficient osteoclastogenic response to RANKL. Furthermore, M-CSF and RANKL both activate mitogen-activated protein kinases (MAPKs), including extracellular signal-regulated kinase 1/2 (ERK1/2), JNK1/2/3, and P38, which are essential for osteoclast differentiation [4].

Homeostasis of the gut microbiome is essential for bone health.

Germ-free mice exhibited increased bone mineral density associated with a reduced number of osteoclasts per bone surface compared with conventionally raised mice [5]. Another study demonstrated that colonization by conventional specific pathogen-free gut microbiota increased both bone formation and resorption in germ-free mice by upregulating insulin-like growth factor-1 (IGF-1). Supplementation of antibiotic-treated mice with short-chain fatty acids (SCFAs), which are products of microbial metabolism, restored IGF-1 and bone mass to the levels observed in control mice [6]. In addition to SCFAs, various gut microbiome-derived metabolites such as bile acids [7], branched-chain amino acids [8,9], and trimethylamine N-oxide [10] have been implicated in regulating bone homeostasis.

Accumulating evidence indicates gut microbiota composition is altered in osteoporotic postmenopausal women. Using shotgun metagenomic sequencing, unclassified *Clostridia* and *Methanobacteriaceae* were found to be less abundant in osteoporotic and osteopenic postmenopausal women than in healthy controls [11]. Another study demonstrated that the abundances of *Proteobacteria* and *Synergistetes* were higher, whereas those of *Bacteroidetes* were lower at the phylum level in the postmenopausal osteopenia group than in the control group [12]. In addition, transplantation of fecal microbiota prepared from healthy C57BL/6 mice prevented the OVX induced bone loss through suppressing osteoclast formation [13], suggesting the critical function of gut microbiota in OVX induced bone loss. However, the molecular mechanism behind the association of altered gut microbiota and postmenopausal osteoporosis (PMO) remains unknown.

Here, we showed that gut *C. spor.* and its derived metabolite IPA were associated with postmenopausal osteoporosis in mouse models. IPA suppressed osteoclast differentiation by inhibiting RANKL-induced PXR ubiquitination and subsequent degradation, which led to increased binding of remaining PXR with P65. *In vivo* IPA gavage or *C. spor.* transplantation protected against OVX-induced bone loss. A convenient *C. spor.*-encapsulated silk fibroin (SF) hydrogel system achieved bone protection similar to IPA gavage or *C. spor.* transplantation. Thus, restoring gut *C. spor.* abundance may be a promising strategy for countering postmenopausal osteoporosis.

2. Methods and materials

2.1. Reagents

IPA (HY-W015229), MG132 (HY-W015229), cycloheximide (CHX) (HY-12320) were purchased from MedChemExpress (NJ, USA). Recombinant M-CSF (#416-mL) and RANKL (#462-TR) were obtained from R&D Systems (Minneapolis, MN, USA). Antibodies against PXR (#ab217375), Ctsk (#ab37259), and Trap (#ab52750) were purchased from Abcam (Cambridge, UK). Antibodies against Nfatc1 (#8032), c-Fos (#2250), P38 (#8690), JNK (#9252), ERK (#4695), P65 (#8242), NF-κB inhibitor α (IκBα) (#4812), p-P38 (#4511), p-JNK (#9255), p-ERK (#4370), p-P65 (#3033), and p-IκBα (#2859) were obtained from Cell Signaling Technology (MA, USA).

2.2. Bone marrow derived macrophages (BMMs) isolation and in vitro osteoclast differentiation assay

As previously reported, BMMs were flushed out from the medullary space of the tibia and femur of 8-week-old C57BL/6 J mice and then cultured in αMEM medium with 30 ng/mL recombinant M-CSF and 10% fetal bovine serum (FBS) [14]. After 12–16 h, the suspended cells were collected and cultured for 3 days. The adherent cells were then dissociated with 0.25% trypsin for further use. For the osteoclast differentiation assay, 20,000 cells were seeded on 96-well plates and cultured in 200 µL αMEM medium containing 30 ng/mL M-CSF, 75 ng/mL RANKL, and 10% FBS with daily media changes for 5 days.

2.3. CCK8 assay

CCK8 assay was performed to evaluate cell proliferation. Briefly, cells were seeded in 96-well culture plates (Corning Life Science) and incubated with IPA for indicated time durations. Then, 10 µL CCK8 reagent was added to the wells and incubated for 1 h. The absorbance was determined at 450 nm using a SpectraMax 190 Microplate Reader (Molecular Devices).

2.4. TUNEL assay

BMMs were seeded at 6000 cells/well in 48-well plates. After incubation for 24 hours, cells were treated with different concentrations of IPA (dissolved in DMSO) for 5 days. The apoptosis rate was assessed at single cell level using a TUNEL staining kit (G3250, Promega, USA). TUNEL-positive cells were visualized under a fluorescence microscope (Leica, Germany). For quantification of apoptosis, cells were counted from 6 random selected views using image J software. The results were presented as a percentage of apoptotic cells over the total number of cells counted.

2.5. TRAP staining, F-actin ring formation analysis, and pit formation assay

A TRAP staining kit (387A–1KT, Sigma) was used to visualize osteoclasts after differentiation, according to the manufacturer's instructions. Briefly, the cells were fixed with 4% paraformaldehyde (PFA) for 10 min and then the staining solution was added. After incubating at 37°C for 1 h, the whole plates were scanned using a microscope (Leica, Munich, Germany), and TRAP-positive multinucleated cells with three or more nuclei were counted as osteoclasts [15].

For the F-actin ring formation assay, BMMs were cultured on the surface of 0.2% collagen gel-coated 6-well plates in the presence of 30 ng/mL M-CSF and 75 ng/mL RANKL for 6 days to induce osteoclast differentiation. Then, the cells were digested with collagenase (0.2%) and seeded onto hydroxyapatite-coated Osteo Assay strip well plates (#3988, Corning, Inc., USA). Thereafter, osteoclasts were treated with various concentrations of IPA in the presence of 30 ng/mL M-CSF and 75 ng/mL RANKL for 2 days, and 4% PFA and 0.1% Triton X-100 were used to fix and permeabilize the cells, respectively. Cells were stained with rhodamine-conjugated phalloidin in 2% bovine serum albumin for 1 h. Nuclei were visualized by DAPI staining for 5 min. Images of three fields were randomly captured using a fluorescence microscope (Leica, Munich, Germany). Three patterns of podosome structures, podosome clusters, actin rings, and podosome belts were counted [16]. ImageJ software was used to quantify the size of F-actin rings.

For pit formation assays, the osteoclasts were induced as described in the F-actin ring formation assay. Then, the cells were digested with collagenase (0.2%) and seeded onto hydroxyapatite-coated Osteo Assay strip well plates. After incubating with media containing 30 ng/mL M-CSF, 75 ng/mL RANKL and various concentrations of IPA for 2 days, the osteoclasts were lysed and washed to expose the bottom from the surface using the 10% bleaching solution, and the resorption pits were captured under a light microscope (Leica, Munich, Germany). The resorption area was analyzed using the ImageJ software (National Institutes of Health).

2.6. Immunofluorescence

Briefly, the cells were fixed in 4% paraformaldehyde for 10 min and permeabilized with 0.2% Triton X-100 (Solarbio, China) for 5 min. Then, the nonspecific binding of the first antibody was blocked by 1% BSA in PBST at room temperature for 1 h. Subsequently, the cells were incubated with diluted primary antibodies under continuous shaking at 4°C overnight. The next day, the cells were washed with PBST three times and incubated with appropriate secondary antibodies in the dark for 1 h, followed by incubation with DAPI (Boster Biological

Technology, China) for 5 min. Finally, images were captured using a fluorescence microscope.

2.7. RT-qPCR

Total mRNA was extracted from cultured cells using the TRIzol reagent (Takara, Japan) according to the manufacturer's protocol. mRNA was reverse-transcribed into cDNA using the HiScript III All-in-one RT SuperMix (Vazyme Biotech Co. Ltd., Nanjing, China), and real-time PCR analyses were performed using the CFX Connect Real-Time System with HiScript II Q RT SuperMix (Vazyme Biotech Co., Ltd., Nanjing, China). The mRNA levels of the target genes were normalized to those of the housekeeping gene β-actin. The primers information is listed in Supplementary Table S1.

2.8. Western blotting assay

After washing twice with phosphate buffered saline (PBS), radio-immunoprecipitation assay (RIPA) buffer containing phosphotransferase inhibitor (1%) and proteinase inhibitor (1%) was used to lyse cultured cells. Proteins (20 μg) were separated by 10% SDS-PAGE and transferred to a polyvinylidene difluoride (PVDF) membrane. The membranes were incubated at 4°C overnight with the indicated primary antibodies. Horseradish peroxidase-conjugated anti-mouse or anti-rabbit IgG (5873 S, CST) was used as a secondary antibody. Chemiluminescence (#34095; Thermo Fisher Scientific, USA) was used to develop signals, which were quantified via densitometry using Quantity One Software (Bio-Rad Laboratories, USA).

2.9. Co-IP (Co-immunoprecipitation) assay

For the Co-IP assay, two million cells were seeded on 6-cm dishes. The cells were treated with the proteasome inhibitor MG132 (0.5 mM) for 4 h before collection. After treatment, the cells were harvested and lysed with specific IP lysis buffer (#P0013, Beyotime, China) containing phosphotransferase inhibitor (1%) and proteinase inhibitor (1%) on ice for 30 min, followed by centrifugation for 5 min at 12,000 rpm at 4°C. The collected lysates were precleared using protein A/G magnetic beads (EngiBody Biotechnology, Shanghai, China). Subsequently, antibodies against the target proteins were mixed with the lysate and incubated at 4°C for 16 h. After four washes with PBS, the co-IP products were collected using protein A/G magnetic beads and analyzed by western blotting.

2.10. IPA measurement

Ten-week-old female C57BL/6J mice were divided into SHAM and OVX groups. Eight weeks after ovariectomy, all mice were sacrificed, and serum was collected. Serum IPA levels were analyzed using an enzyme-linked immunosorbent assay kit (#CB11098-Mu, COIBO BIO, China) following the manufacturer's instructions.

2.11. RNA sequencing and analysis

BMMs were divided into IPA-treated and control groups, with four replicates in each group. Total RNA was extracted using an RNAeasy Kit (Qiagen, Germany) according to the manufacturer's guidelines. A total amount of 5 μg of RNA per sample was used as input material for the RNA sample preparations, with mRNA purified from total RNA using poly-T oligo-attached magnetic beads. Following the manufacturer's recommendations (Novogene Co., LTD, China), sequencing libraries were constructed using the NEBNext® UltraTM RNA Library Prep Kit for Illumina® (NEB, USA). Sequencing reads were aligned to the mouse reference genome mm10 (GRCm38.90) using the STAR aligner (v2.5.1b) guided by the mouse GENCODE gene model release v15. HTSeqv0.6.0 was used to count the read numbers mapped to each gene. The

fragments per kilobase of transcript per million mapped reads (FPKM) of each gene were calculated based on the length of the gene and the read count mapped to the gene. Raw count data were normalized using the voom function in the R limma package and differential expression analysis was performed using the limma package. DEGs were defined as having at least a 1-fold change in expression and adjusted $P < 0.05$ in comparisons of different genotypes.

2.12. Lentivirus transfection

Three short hairpin RNAs (shRNAs) against PXR and a scrambled control lentivirus were purchased from ViGene Biosciences, Inc. The sequences of the shRNAs were as follows: shRNA1, 5'-GGGCCTTGAT-CAAGAGGAAGATTCAAGAGATCTTCCTCTTGATCAAGGCCCTTTTTT-3', shRNA2, 5'-GCTACCACTTCAATGTCATTTCAAGAGAATGACATTG AAGTGGTAGCTTTTTT-3', shRNA3, 5'-GCACAACTTTCTCCCACTTCAA TTCAAGAGATTGAAGTGGGAGAAAGTTGTGTTTTTT-3'.

The PXR-overexpressing lentivirus was constructed by Shanghai GeneChem Co. Ltd. (Shanghai, China). The sequence of PXR was obtained from NCBI (All Resources – Site Guide – NCBI; https://www.nih. gov/) and subcloned into a lentivirus vector to overexpress PXR (Over-PXR); the green fluorescent protein (GFP) vector was used as a negative control. The primers used to obtain target DNA fragments and identify recombinant DNA clones are as follows: Forward, 5'- CACACTGGAC-TAGTGGATCCCGCCACCATGAGACCTGAGGAGAGCTG-3'; Reverse, 5'-AGTCACTTAAGCTTGGTACCGAGCCATCTGTGCTGCTAAATAACTC-3'. BMMs were incubated with lentivirus in a complete αMEM medium containing 5 μg/mL polybrene (Thermo Fisher) for 24 h. Subsequently, the cells were harvested to determine the knockdown or overexpression efficiency of each shRNA by qPCR and western blotting.

2.13. 16S rRNA sequencing

Fecal samples were processed by Shanghai Majorbio Bio-Pharm Technology Co., Ltd. (Shanghai, China). Total bacterial DNA from the feces was extracted, amplified, and sequenced according to standard procedures. Briefly, microbial DNA was extracted using the E.Z.N.A.® Soil DNA Kit (Omega Bio-tek, Norcross, GA, U.S.) according to the manufacturer's protocol. DNA concentration was assessed using a Nanodrop spectrophotometer (Thermo Scientific, USA) and quality was determined by agarose gel electrophoresis. Bacterial 16 S rRNA gene sequences spanning the variable regions V4-V5 were amplified using primers 338 F and 806 R. The amplicons were then extracted from 2% agarose gels and further purified using the AxyPrep DNA Gel Extraction Kit (Axygen Biosciences, CA, U.S.) and quantified by QuantiFluor™-ST (Promega, U.S.). Purified amplicons were pooled in equimolar amounts and subjected to paired-end sequencing (2×300 bp) on an Illumina MiSeq platform.

Raw FASTQ files were de-multiplexed using an in-house Perl script, and then quality-filtered by fastp version 0.19.6 and merged by FLASH version 1.2.7, with the following criteria: (i) the 300 bp reads were truncated at any site receiving an average quality score of <20 over a 50 bp sliding window, and the truncated reads shorter than 50 bp were discarded; reads containing ambiguous characters were also discarded; (ii) only overlapping sequences longer than 10 bp were assembled according to their overlapping sequence. The maximum mismatch ratio in the overlapping region was 0.2. Reads that could not be assembled were discarded; (iii) Samples were distinguished according to the barcode and primers, and the sequence direction was adjusted, exact barcode matching, and two nucleotide mismatches in primer matching. Then the optimized sequences were clustered into OTUs using UPARSE 7.1 with a 97% sequence similarity level. The most abundant sequence of each OTU was selected as the representative sequence. To minimize the effects of sequencing depth on alpha and beta diversity measures, the number of 16 S rRNA gene sequences from each sample was rarefied to 20,000, which still yielded an average Good's coverage of 99.09%,

respectively. Raw sequencing data were accessible at NCBI Bioprojects under PRJNA1039494.

2.14. TaqMan real-time PCR

Specific TaqMan real-time PCR for *C. spor.* was performed according to the manufacturer's instructions. A broad-range real-time PCR PP-BioMole-083 assay was used as recommended by the manufacturer. The specific primers and probe were used: Forward, 5'-TTAA-TACCGCATAACATAAGAGAA-3'; Reverse, 5'-CCAGAAAA-CAGGGCTTTAC-3'; probe, FAM-ATTGCTTTGAGATGGACCCGCG-LFN. Thermal cycling was performed using the ABI PRISM 7500 detection system (Applied Biosystems, USA) as follows: 2 min at 50°C for the uracil-N-glycosylase reaction, 2 min at 95°C for denaturation, followed by 10 cycles of 15 s at 95°C, 30 s at 55°C, and 30 s at 72°C, followed by 35 cycles of 15 s at 95°C and 1 min at 60°C.

2.15. Fabrication and characterization of bacteria-encapsulated SF hydrogel

Silk fibroin (SF) was prepared using a typical dissolution method. First, the degumming process of silkworm cocoons was operated in an Na_2CO_3 aqueous solution (0.5%, w/v) boiled three times for 20 min each time. The boiled products were rinsed thoroughly with deionized (DI) water until the degummed sericin was completely removed. Then, the degummed SF was fully dried at 40°C for 24 h, and the dried raw SF was dissolved in Ajisawa's reagent, composed of $CaCl_2$: ethanol: H_2O (1:2:8 in molar ratio), for 2 h at 90°C. The dissolved SF solution was centrifuged at 8000 rpm for 20 min to remove insoluble impurities and aggregates. The collected SF solution was dialyzed against DI water for at least three days (MWCO = 3000 Da). The final SF solution was lyophilized and stored at 4°C.

Bacteria were cultured overnight and suspended at a ratio of 1:100 in liquid culture medium. SF solution (5%, w/v) was prepared and completely mixed with the above liquid at a volume ratio of 10:1. Next, the mixed solution was sonicated for 30 s at 10% energy power, yielding the injectable **B@SF hydrogel**. Pristine **SF hydrogel** was fabricated as a control.

The morphology and distribution of bacteria in the hydrogels were observed using SEM, JEOL JSM-6510LV, Tokyo, Japan). The viscoelastic behavior of the hydrogel was measured using the Discovery HR-20 Rheometer (AR2000, TA Instruments, USA). The examinations were operated in a parallel-plate model (25-mm diameter) with a 1-mm gap at 37°C. For the time sweep test, the strain and frequency were fixed at 1% and 1 rad/s, respectively. As for the strain sweep test, the frequency was fixed at 1 rad/s, and the stress ranged from 0.1% to 1000%. For the frequency sweep test, the strain was fixed at 1%, and the frequency ranged from 0.1 to 100 rad/s.

2.16. Biodistribution of SF hydrogels in the gastrointestinal tract (GIT)

Cy5.5-conjugated SF was prepared using a chemical coupling method and used for hydrogel fabrication. The grafted Cy5.5-SF hydrogel was administered to mice by oral gavage. At different time points after oral gavage (2, 6, 12, and 24 h), the mice were euthanized, and the whole GIT was excised. GIT fluorescence imaging was performed using the Kodak In-Vivo FX Professional Imaging System (CT, USA) to detect the biodistribution of hydrogel in the GIT.

2.17. Mouse model of ovariectomy (OVX) and in vivo treatment

Animal experiments were approved by the Ethics Committee of Tongji Hospital, Huazhong University of Science and Technology (No. TJ20200056) and performed following the guidelines of WMA Statement on animal use. Eight-week-old C57BL/6 J female mice weighing 20 ± 2 g were randomly divided into five groups of six mice each:

SHAM+VEHICLE (corn oil); OVX+VEHICLE; OVX+IPA (10 mg/kg body weight); OVX+*C. spor.*; and OVX+ *C. spor.* + tryptophan enriched diet (2.6 g/kg tryptophan). As reported previously, the OVX model was constructed by removing both ovaries using a dorsal approach. For mice in the SHAM group, the incision was sutured directly after ovarian exposure. One week after surgery, the mice were intragastrically administered IPA or vehicle 7 days a week for 6 weeks. For *C. spor.* recolonization, as previously reported for *C. spor.* (ATCC15579), the bacteria were cultured anaerobically overnight in trypticase yeast extract medium. The bacterial cultures were mixed with glycerol in hermetically sealed glass vials to obtain a final concentration of 10×10^6 CFU/mL for *C. spor. C. spor.* were transplanted into the cecum by oral gavage for 15 consecutive days at a density of 1×10^6 CFU per day.

2.18. Measurement of liver function and kidney function markers

Serum biochemical markers including level of total bilirubin (T-bil), creatinine (CRE), urea (UREA) and activity of alanine aminotransferase (ALT) and aspartate aminotransferase (AST) were measured by Rayto Chemray 800 machine. These parameters were determined according to the methods described previously [17].

2.19. μCT and histomorphometric analysis

μCT (Scanco Medical, Switzerland) scanning was performed with the parameters of 100 kV, 98 μA, and 10-μm voxel size. Trabecular bone morphometric parameters included BMD (bone mineral density), BV/TV, Tb.N, Tb.Sp, and Tb.Th.

For histomorphometric analysis, femur samples were fixed in 4% PFA for 48 h, followed by decalcification in 15% ethylenediaminetetraacetic acid (EDTA) for 2 weeks and then embedded in paraffin. Subsequently, the femurs were sectioned into slices (6 μm) for TRAP and H&E staining. TRAP-positive cells with three or more nuclei were quantified using the ImageJ software before calculating Oc.S/BS (%).

2.20. Statistical analysis

All data representative of three independent experiments are presented as mean ± SEM. Two-tailed t-tests were conducted to determine the significance between the two groups. One or two-way analysis of variance with Bonferroni post hoc tests was conducted for multiple groups using GraphPad Prism version 5. For all statistical tests, a P-value < 0.05 was considered statistically significant.

3. Results

3.1. C. spor. and its derived IPA are decreased in ovariectomized mice

Ovariectomy mice models were first established to simulate postmenopausal women. As expected, a dramatic decrease in the bone volume to total volume (BV/TV), bone mineral density (BMD), trabecular number (Tb.N), and trabecular thickness (Tb.Th) was observed in the OVX group compared with the SHAM group (Figs. 1A and S1). In contrast, trabecular spacing (Tb.Sp) increased. To determine the changes in gut microbiome induced by ovariectomy, fecal samples were collected for 16 S RNA sequencing. Principal component analysis (PCA) explained 22.14% of the total variation in bacterial operational taxonomic units (OTUs), including 13.8% of principal component 1 (PC1) and 8.34% of principal component 2 (PC2), respectively. At the same time, distinct separation along PC1 and PC2 was observed between samples from the OVX and SHAM mice (Fig. 1B). Moreover, Welch's t-test calculated for the Shannon index indicated a significant difference, with a P-value of 0.0038 in the OTU level of gut microbiome distribution between OVX and SHAM mice (Fig. 1C). At the class level, heatmap analysis of the differential flora in both groups revealed that the most
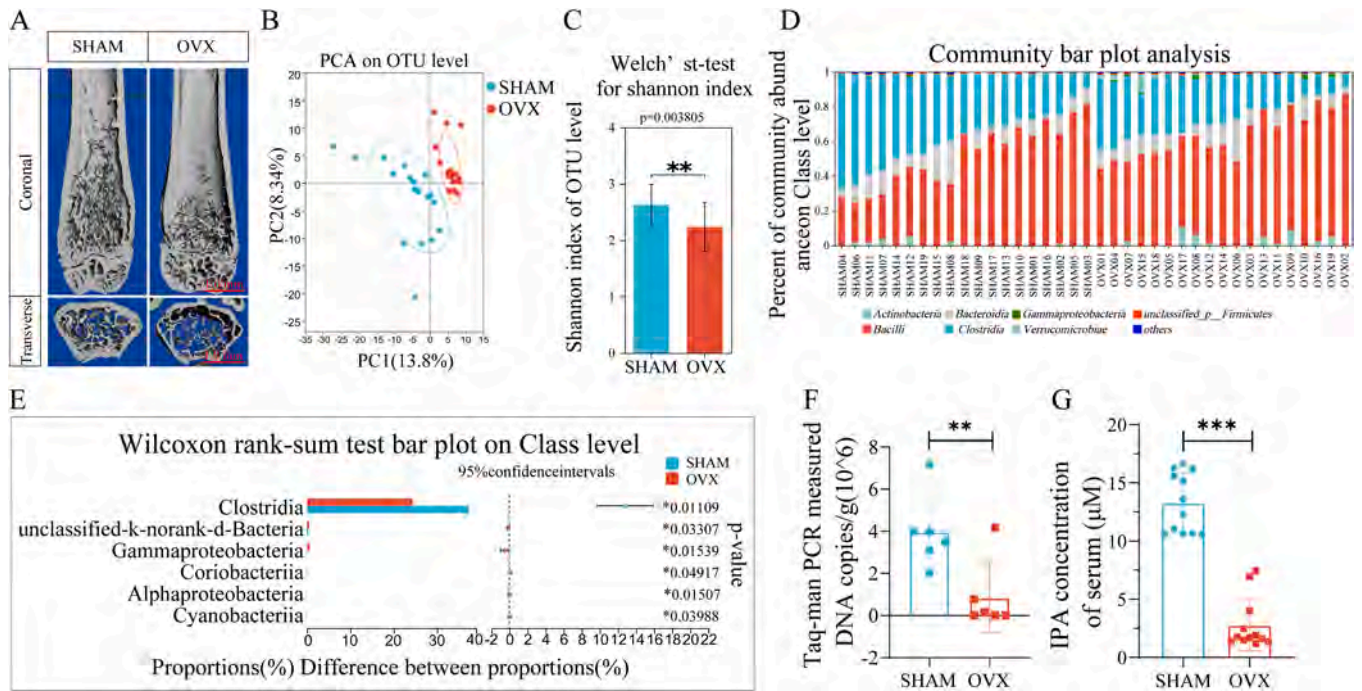
Fig. 1. *C. spor.* and its derived IPA are decreased in ovariectomized mice. (A) Representative 3D-reconstructed images of the distal femurs of mice from the OVX and SHAM groups. Red scale bar refers to 1.0 mm. (B) Principal component analysis (PCA) showing differences in the gut microbiome of stool samples from 19 SHAM (SHAM, blue) and 19 OVX (OVX, red) mice. (C) Shannon index of Welch's t-test showing differences in the gut microbiome of stool samples from SHAM and OVX mice. (D) Comparison of class-level proportional abundance of the gut microbiome in stool samples from SHAM (SHAM, blue) and OVX mice (OVX, red). (E) Wilcoxon rank-sum test identified six gut microbiomes in stool samples at the class level. (F) Taq-man PCR for DNA copied of *C. spor.* in fecal samples from SHAM and OVX mice. (G) IPA levels in the serum of SHAM mice and OVX mice measured by ELISA. Data are shown as mean ± SEM. * P < 0.05, ** P < 0.01, and *** P < 0.001.

abundant bacterial genera were *Bacilli*, *Clostridia*, and *Bacteroidia*. Interestingly, the abundance of *Bacilli* was increased in OVX mice (Fig. 1D-E). In contrast, the abundance of *Clostridia* was decreased, consistent with the results of a previous study conducted in humans [11]. The Wilcoxon rank-sum test bar plot at the class level also confirmed that the abundance of *Clostridia* was significantly decreased in OVX mice.

C. spor. among *Clostridia* metabolizes tryptophan to IPA in the gut [18]. Previous studies reveal the critical role of tryptophan metabolism in bone homeostasis [19]. Therefore, we asked whether *C. spor.* and its derived metabolite were changed in the gut of OVX mice. Real-time PCR was conducted to determine the abundance of *C. spor.*, which revealed that the abundance of *C. spor.* was decreased in the OVX group (Fig. 1F). Meanwhile, compared with SHAM mice, serum concentrations of IPA of OVX mice were reduced by nearly 80% (Fig. 1G). Pearson's correlation analysis between BV/TV and IPA concentrations suggested IPA concentrations were well correlated with BV/TV (Fig. S1). Taken together, these findings revealed that ovariectomy was associated with decreased abundance of *C. spor.* in the gut and downregulated serum IPA.

3.2. IPA inhibits osteoclast differentiation and bone resorption

The pathogenesis of postmenopausal osteoporosis is featured by increased osteoclast number and activity [20]. To determine the potential role of IPA in osteoclast formation, osteoclast differentiation assays were performed with and without IPA treatment. Tartrate-resistant acid phosphatase (TRAP) staining results suggested that TRAP-positive cells with multiple nuclei or osteoclasts formed well in the control group after stimulation with M-CSF and RANKL. In contrast, few osteoclasts were observed in the 12.5 μM IPA treatment group; the changes were more obvious in the 25 μM IPA treatment group. In the 50 μM IPA group, the osteoclast suppression effect was further enhanced (Fig. 2A-B). Consistent with the osteoclast differentiation assays, actin

ring formation, as visualized by phalloidin staining, was also inhibited by IPA treatment in a concentration-dependent manner (Fig. 2C). The quantified podosome counts based on phalloidin staining exhibited a significant decrease from 0 μM to 50 μM IPA treatment (Fig. 2D). CCK8 assay and TUNEL staining demonstrated that IPA treatment did not affect cell proliferation or cell apoptosis in BMMs, which excluded the possibility that the suppressive effect of IPA on osteoclast differentiation resulted from decreased cell proliferation or increased apoptosis of BMMs (Fig. S2). Bone resorption assays showed the resorption area was decreased from 28% in the dimethyl sulfoxide (DMSO) group to 3% in the 50 μM IPA group, which indicated that IPA suppressed osteoclast bone resorption (Fig. 2E-F).

Expression levels of osteoclast marker genes and master regulators were also investigated. Molecular analysis by quantitative reverse transcription PCR (RT-qPCR) revealed that the expression of osteoclast markers matrix metallopeptidase 9 (Mmp9), cathepsin K (Ctsk), Trap, and nuclear factor of activated T cells 1 (Nfatc1) was suppressed in the IPA treatment groups in a concentration-dependent manner (Fig. 2H-K). Western blotting further revealed decreased protein levels of c-Fos and Nfatc1, two master regulators of osteoclast differentiation, in the IPA-treated groups. The protein levels of other osteoclast markers, such as Mmp9, Trap, and Ctsk, also decreased (Fig. 2L-P), consistent with the RT-qPCR data. Thus, IPA suppressed RANKL induced expression of osteoclast markers at both mRNA and protein level. Time-interval incubations revealed that c-Fos was significantly suppressed by IPA after 1-day incubation with RANKL and IPA compared with incubation with RANKL alone, which indicated suppression of c-Fos expression was an early effect triggered by IPA treatment. This suppression effect decreased with time. In contrast, the expression of Mmp9, Trap, and Nfatc1 was obviously decreased after 5 days of incubation with RANKL and IPA (Fig. 2Q-U). Overall, the *in vitro* assays suggested IPA suppressed osteoclast formation and function in a dose-dependent way, which was confirmed by expression changes of c-Fos, Mmp9, Ctsk and Nfatc1.
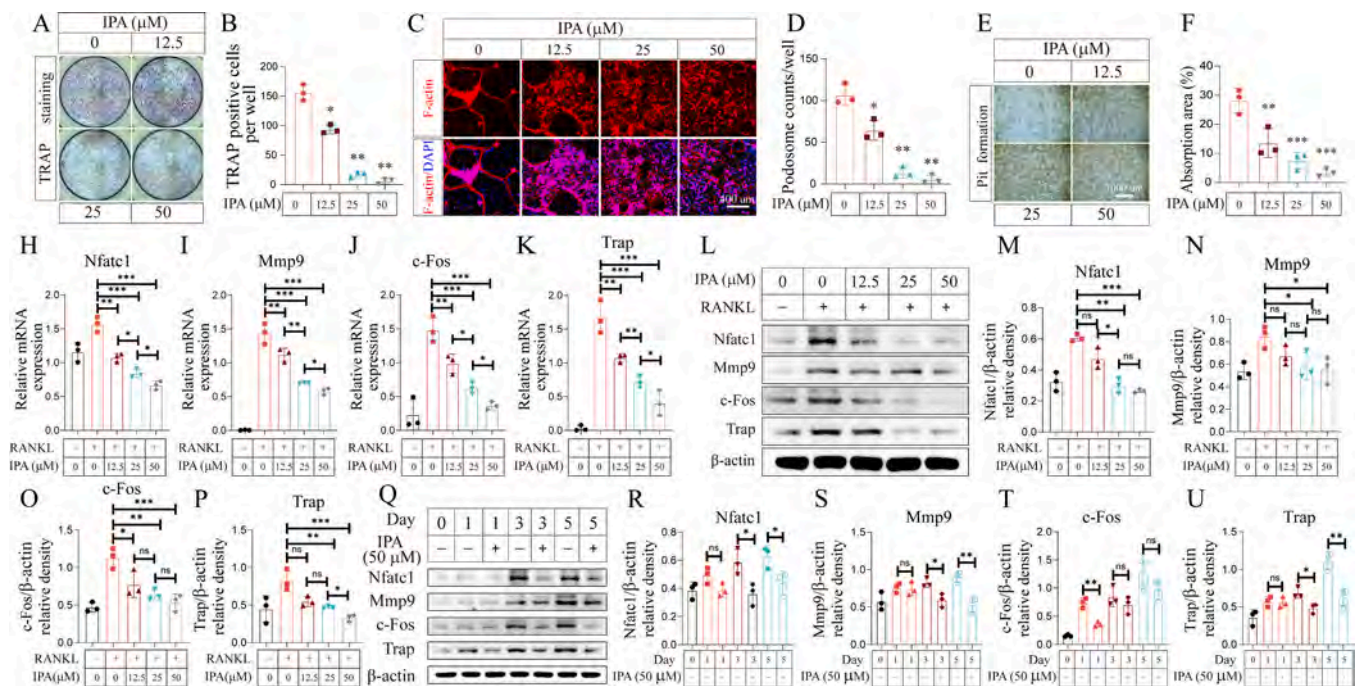
Fig. 2. IPA inhibits osteoclast differentiation and bone resorption. (A, B) IPA suppressed RANKL-induced osteoclastogenesis in a concentration-dependent manner. BMMs were treated with different concentrations of IPA (0, 12.5, 25, and 50 μM), with induction by M-CSF and RANKL for 5 days. TRAP-positive multinucleated (> 3 nuclei) cells were counted as osteoclasts. (C, D) BMMs were seeded on 0.2% collagen-gel-coated six-well plates and stimulated with 30 ng/mL M-CSF and 75 ng/mL RANKL for 6 days. Then, the cells were digested and seeded onto the Osteo Assay strip well plates. Mature osteoclasts were treated with various concentrations of IPA for 2 days. F-actin staining was performed, and three patterns of podosome—podosome clusters, actin rings, and podosome belts—were counted. (E, F) Mature osteoclasts were cultured on Osteo Assay strip well plates and treated with the medium containing M-CSF and RANKL in combination with various concentrations of IPA for 3 days. The cells were then washed from the surface by using 10% bleaching solution for 5 min. Resorption pits were captured with light microscopy and analyzed using Image J software. (H-K) BMMs were cultured with the medium containing M-CSF, RANKL, and IPA of a series of concentrations for 5 days. Relative mRNA expression levels of Nfatc1, Mmp9, c-Fos, and Trap versus β-actin were quantified using qPCR. (L-P) BMMs were treated with indicated concentrations of IPA (0, 12.5, 25, and 50 μM) with stimulation by M-CSF and RANKL for 3 days, and protein expression of osteoclast-specific genes was determined using Western blot followed by quantification of bands intensity. (Q-U) BMMs were treated with indicated concentrations of IPA (50 μM) with stimulation by M-CSF and RANKL for 0, 1, 3, and 5 days. The protein expression of osteoclast-specific genes was determined using Western blot followed by quantification of bands intensity. $*P < 0.05$, $**P < 0.01$ and $*** P < 0.001$. NS, no significance.

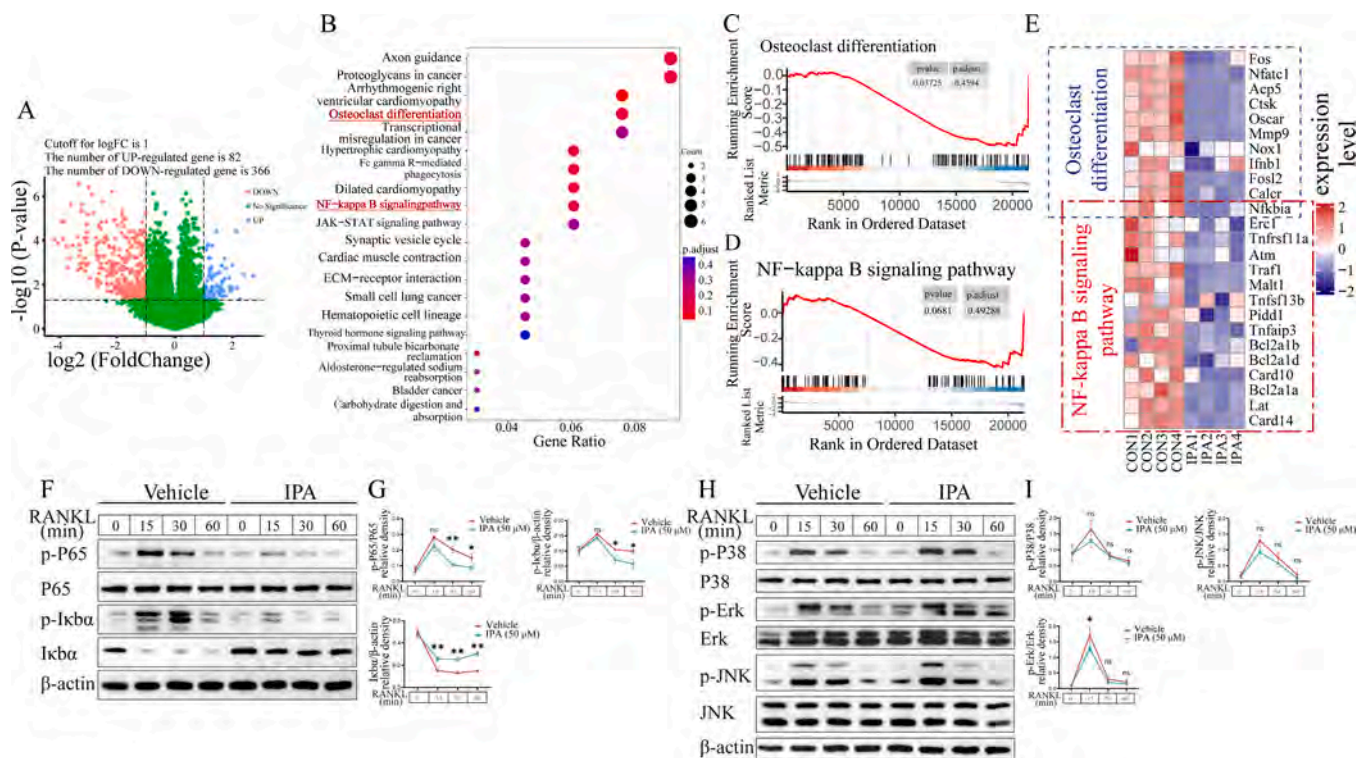### 3.3. IPA suppresses RANKL-induced NF-κB but not MAPK activation

RNA sequencing was performed to profile transcriptomic changes associated with IPA-induced osteoclast suppression. A total of 448 differentially expressed genes (DEGs) were identified, 366 of which were downregulated by more than two-fold, whereas 82 DEGs were upregulated (Fig. 3A). The Kyoto Encyclopedia of Genes and Genomes (KEGG) analysis of DEGs identified significantly altered pathways such as axon guidance and proteoglycans in cancer (Fig. 3B). Among these significantly altered pathways, osteoclast differentiation and NF-κB pathways, which are reported to be critical in osteoclast formation [21], attracted our attention (Fig. 3C-D). In the osteoclast differentiation pathway, the expression of Fos, Nfatc1, Ctsk, osteoclast-associated receptor (Oscar), and Mmp9 was obviously decreased in the IPA treatment group, consistent with our previous RT-qPCR and western blotting data. Meanwhile, Tnfrsf11a, Traf1, Malt1, Tnfaip3, Bcl2a1a, Lat, and Carrd14 in NF-κB pathway were downregulated in the IPA treatment group (Fig. 3E). These findings indicated that the NF-κB pathway might participate in IPA-induced changes in osteoclast differentiation.

NF-κB and MAPK are two critical pathways activated by RANKL/ RANK interaction [21]. To assess potential changes in the activation of NF-κB and MAPK pathways induced by IPA, cells were starved in serum-free media and pretreated with IPA for 16 h, followed by RANKL treatment for the indicated time intervals in Fig. 3F-I. As expected, phosphorylation of P65 by IκBα was dramatically increased after 15 min of incubation with RANKL. However, as shown by quantified p-P65 to total P65 and p-IκBα to total IκBα data, RANKL-induced changes were

decreased by IPA treatment (Fig. 3F-G). In contrast, IPA pretreatment did not change the RANKL-induced p-P38, p-ERK, or p-JNK (Fig. 3H-I). The data demonstrated that NF-κB, but not MAPK, was involved in IPA treatment-induced osteoclast suppression.

3.4. IPA suppresses osteoclast differentiation by activating PXR

PXR is a receptor of IPA according to previous studies [22,23]. To determine the potential role of PXR in IPA-induced osteoclast suppression, RT-qPCR for genes downstream of PXR, including CYP3a11, MDR1, and UGT1a1, was performed. CYP3a11 and MDR1 were upregulated by 12.5 μM IPA treatment (Fig. S3), indicating that PXR was activated by IPA. With 25 μM IPA, their expression was further promoted. In addition, UGT1a1 was also upregulated. To determine the function of PXR in osteoclast differentiation, we first evaluated changes in PXR expression during osteoclast formation. PXR expression decreased from day 0 to day 1 during osteoclast differentiation at both the mRNA and protein levels and remained low thereafter (Fig. 4A-B). To further assess whether the inhibition of osteoclasts by IPA occurred by activating PXR, we constructed an shRNA targeting PXR (sh-PXR). The knockdown efficiency of sh-PXR was assessed using RT-qPCR and western blotting analysis (Fig. S4A-B). TRAP staining suggested that the inhibitory effect of IPA on osteoclast differentiation was abrogated by PXR silencing (Fig. 4C-D). Similarly, F-actin ring formation was restored by sh-PXR (Fig. 4E-F). In addition, IPA-induced inhibition of osteoclast resorption was eliminated (Fig. 4G-H). Further biochemical assays confirmed that sh-PXR rescued the IPA-induced downregulation of

Fig. 3. IPA suppresses RANKL-induced NF-κB but not MAPK activation. (A) Volcano plot showing differentially expressed genes between the control and IPA treatment groups. A total of 82 upregulated and 366 downregulated genes were identified by setting the threshold of log2 (fold change) to 1 and the P-value to 0.05. (B) KEGG enrichment analysis showed various signaling pathways were significantly altered after IPA treatment. (C, D) GSEA analysis confirmed the inhibition of the osteoclast differentiation and NF-kappa B signaling pathways by IPA. (E) Heatmaps showed the downregulated genes in the osteoclast differentiation and NF-kappa B signaling pathways. (F-I) Western blot assay detected RANKL-induced phosphorylation of P65 and IκBα of the NF-kappa B signaling pathway and JNK, ERK, and P38 of the MAPK pathway after IPA pretreatment. * $P < 0.05$; ** $P < 0.01$; *** $P < 0.001$; NS, no significance.

osteoclast markers, including Nfatc1, Mmp9, c-Fos, and Trap, at both the mRNA (Fig. 4I-L) and protein (Fig. 4M-Q) levels. Thus, IPA inhibits osteoclast differentiation and function by activating PXR.

3.5. IPA inhibits the release of P65 from PXR by suppressing PXR ubiquitination

To elucidate the function of PXR in osteoclast differentiation, we constructed a PXR-overexpressing plasmid (over-PXR) (Fig. S5A). PXR overexpression directly inhibited osteoclast differentiation and suppressed F-actin ring formation (Fig. 5A-D). In addition, PXR overexpression significantly inhibited bone resorption by osteoclasts (Fig. 5E-F). Further, RT-qPCR and western blotting experiments showed that PXR overexpression suppressed the expression of RANKL-induced osteoclast markers, including Nfatc1, Mmp9, c-Fos, and Trap (Fig. 5G-K). Meanwhile, RANKL-induced NF-κB activation was suppressed by PXR overexpression, as indicated by decreased phosphorylation of P65 and IκBα at 15 and 30 min after RANKL incubation (Figs. 5L and S5B-D).

Our previous results revealed a significant decrease in PXR expression after 1 day of incubation with RANKL, and it remained at a low level, raising the question of whether changes in PXR expression upon RANKL stimulation were initiated earlier. A short time-point assay demonstrated that PXR was downregulated as soon as 15 min/30 min/ 1 h after RANKL incubation. However, IPA treatment blocked this process, indicating a potential post-translational modification mechanism (Fig. 5M). Human PXR can be ubiquitinated, leading to proteasome-related degradation, which suggests that ubiquitination is responsible for RANKL-induced PXR decrease at the protein level [24]. To investigate the possibility, BMMs pretreated with 50 μM IPA or DMSO for 12 hours were subsequently incubated with CHX for 2, 4 and 6 hours in the presence of IPA or DMSO. The CHX chase assay showed that PXR

protein abundance decreased dramatically in the DMSO group after 2 hours of CHX incubation, indicating a high turnover of PXR in BMMs. In contrast, PXR abundance remained at relatively high level until 6 hours of CHX treatment in the IPA pretreatment group (Fig. S6A). Thereafter, PXR was pulled down, followed by western blotting analysis for ubiquitination. The data suggested that RANKL treatment increased the ubiquitination of PXR, whereas IPA treatment attenuated this change (Fig. 5P). Furthermore, it has been shown that NF-κB P65 disrupts the association of the PXR-RXRα (Retinoid X Receptor Alpha) complex by interacting with the DNA-binding domain of RXRα [25]. Therefore, we investigated whether PXR interacted with P65. Co-immunoprecipitation (co-IP) assays showed that PXR bound to P65, which is different from previous findings for the PXR.RXRα complex [25]. We also found that RANKL treatment decreased PXR-bound P65 (Fig. 5Q). In contrast, IPA treatment restored the binding of PXR with P65. Moreover, immunofluorescence experiments showed that RANKL stimulation decreased PXR expression and reduced the overlap of P65 with PXR (Figs. 5R and S6B). IPA treatment restored PXR expression and promoted its overlapping with P65. These findings demonstrate that IPA activates PXR, leading to decreased RANKL induced PXR ubiquitination and PXR degradation. Subsequently increased P65 is anchored by the remaining PXR, which leads to suppressed osteoclast differentiation.

3.6. Both IPA supplementation and C. spor. colonization protect mice against OVX-induced bone loss

Our *in vitro* experiments revealed that IPA suppressed osteoclast formation and function. OVX treatment led to a significant reduction in the abundance of *C. spor.* in the gut and its derived IPA in the serum, prompting us to investigate the *in vivo* effects of *C. spor.* or IPA supplementation on OVX-induced osteoporosis. To address this question, mice
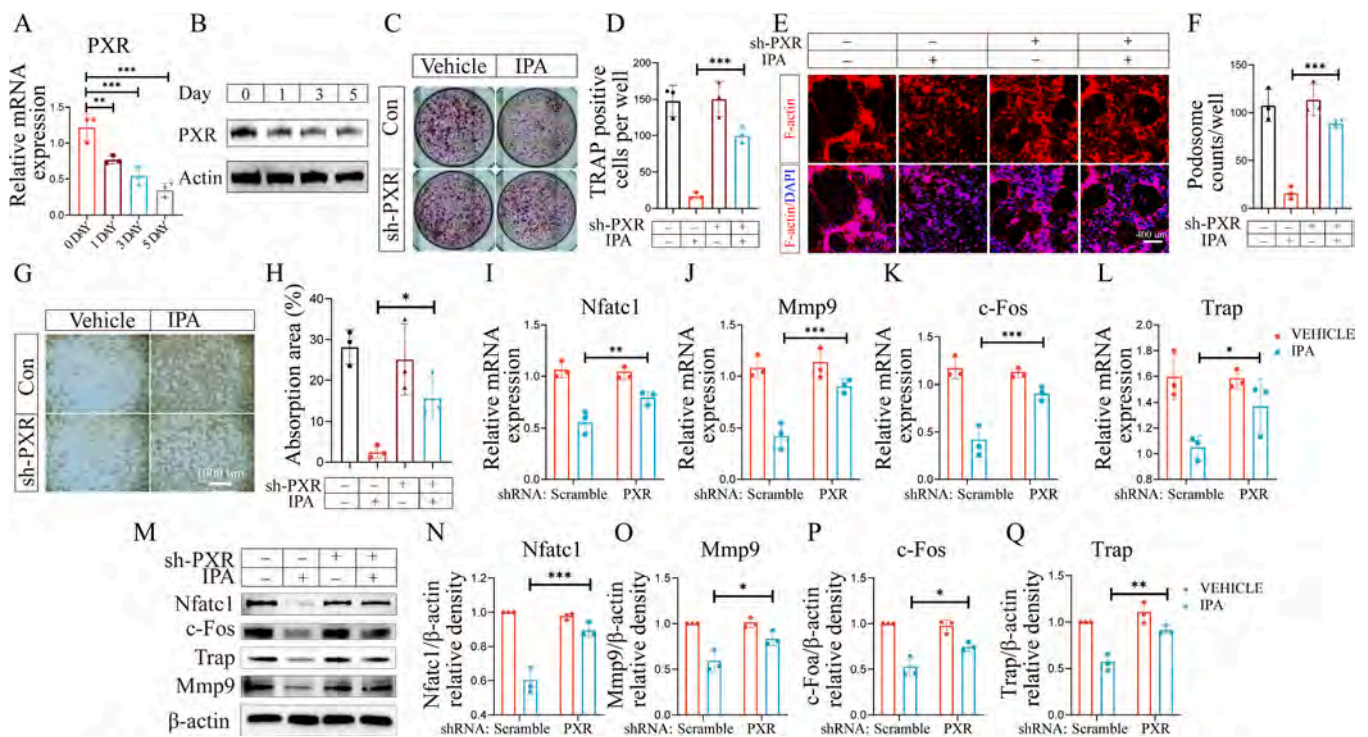
Fig. 4. IPA suppresses OC differentiation through activating PXR. (A, B) BMMs were treated with RANKL for the indicated times (day 0, 1, 3, and 5). The mRNA and protein expression of PXR were determined using qPCR and Western blotting, respectively. (C, D) BMMs were infected with the lentivirus carrying PXR shRNA or the control lentivirus and then cultured in the presence of M-CSF and RANKL for 5 days with or without IPA (50 μM) treatment, followed by TRAP staining. TRAP-positive cells with three or more nuclei were counted as osteoclasts. (E, F) BMMs were seeded onto the Osteo Assay strip well plates and infected with the lentivirus carrying PXR shRNA or the control lentivirus and then cultured in the presence of M-CSF and RANKL for 5 days with or without IPA (50 μM) treatment. F-actin was visualized using phalloidin staining, and three patterns of podosomes—including podosome clusters, actin rings, and podosome belts—were counted. (G, H) BMMs were treated as described in (E, F); the cells were then washed from the surface by using 10% bleaching solution for 5 min. Resorption pits were captured with light microscopy and analyzed using Image J software. (I-L) BMMs were seeded on six-well plates and infected with the lentivirus carrying PXR shRNA or the control lentivirus and then cultured in the presence of M-CSF and RANKL for 5 days with or without IPA (50 μM) treatment. Relative mRNA expression of osteoclast-specific genes was quantified using qPCR. (M-Q) BMMs were treated as described in (I-L). Protein levels of osteoclast-specific genes and PXR were determined using Western blotting. * $P < 0.05$; ** $P < 0.01$; *** $P < 0.001$; NS, no significance.

were randomly divided into five groups. The OVX mice were treated with vehicle (corn oil) or IPA (10 mg/kg body weight) daily via oral gavage for 42 days. The other OVX mice were administered *C. spor.* colonization with or without additional tryptophan supplementation in the diet (Fig. 6A).

Serum IPA levels confirmed that *C. spor.* colonization for 15 consecutive days was effectively upregulated IPA in circulation, and additional tryptophan supplementation in the diet further enhanced it (Fig. 6B). Microcomputed tomography (μCT) scanning suggested a dramatic decrease in the trabecular bone fraction (BV/TV) and BMD in OVX mice treated with the vehicle compared with that in SHAM mice (Fig. 6C). The decrease in bone mass resulted from decreased Tb.N and Tb.Th and increased Tb.Sp (Fig. 6C). As expected, the OVX mice showed significant body weight gain compared to SHAM mice. However, IPA administration or *C. spor.* colonization did not change the body weight gain in OVX mice, which indicate the safety of the treatments (Fig. S7). Further serum biochemical markers of liver function and kidney function including T-bil (total bilirubin), CRE (creatinine), UREA (urea) and activity of ALT (alanine aminotransferase) and AST (aspartate aminotransferase) confirmed the safety of IPA administration and *C. spor.* colonization (Fig. S7). Importantly, OVX mice treated with IPA exhibited a significant increase in BV/TV and BMD compared with OVX mice treated with vehicle (Figs. 6C-G and S7B), indicating that IPA treatment protected OVX mice from bone loss. Interestingly, BV/TV of the *C. spor.* colonization group was higher than that of the SHAM group but not as effective as that with IPA treatment. Additional tryptophan supplementation in the diet resulted in an additional increase in bone volume

in conjunction with *C. spor.* colonization, compared with *C. spor.* colonization alone, which could be explained by increased IPA in the serum (Fig. 6B).

Furthermore, TRAP and H&E staining of the bone sections indicated an increased osteoclast surface/bone surface ratio (Oc.S/BS) in mice in the OVX + VEH group compared with that in mice in the SHAM+ VEH group. However, Oc.S/BS decreased following IPA treatment and *C. spor.* colonization (Fig. 6H-J). Moreover, the combination of *C. spor.* colonization and tryptophan supplementation provided better protection against OVX-induced osteoclast increases than *C. spor.* colonization alone. To determine the potential contribution of bone formation to the gain of bone mass in IPA administration or *C. spor.* colonization, osteoblast differentiation assays using MC3T3-E1 cells were performed. The alizarin red staining and RT-qPCR of osteoblast marker genes suggested IPA treatment did not change osteoblast differentiation (Fig. S8). In addition, toluidine blue staining of the bone sections indicated an increased osteoblast number per bone perimeter (N.Ob/B.Pm(1/mm)) and osteoblast surface/bone surface ratio (Ob.S/BS) in OVX mice compared to SHAM mice, which is consistent with previous study [26]. However, IPA administration or *C. spor.* colonization did not affect N.Ob/B.Pm or Ob.S/BS (Fig. S9).

In summary, both IPA treatment for 42 days and *C. spor.* colonization for 15 days, in combination with additional tryptophan supplementation, prevent ovariectomy-induced bone loss by suppressing osteoclast formation, but do not affect osteoblasts mediated bone formation.
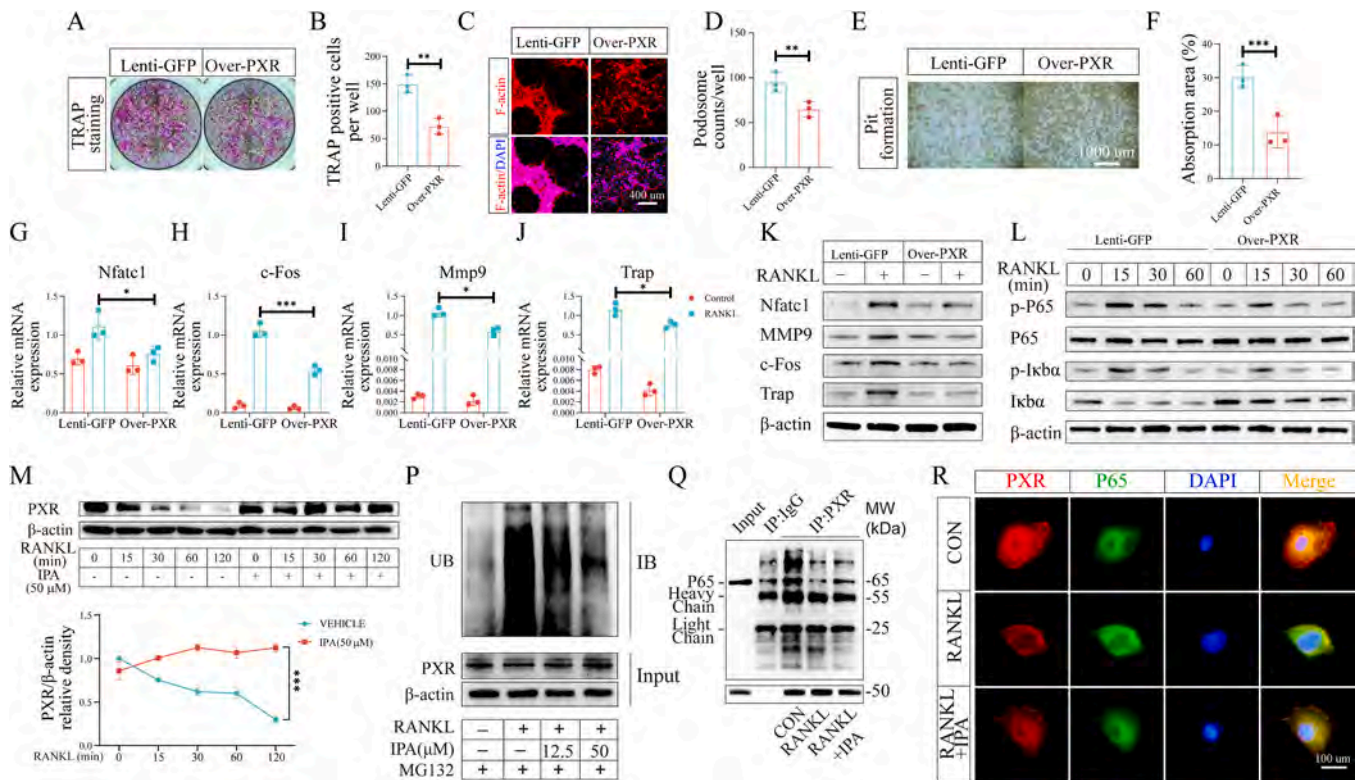
Fig. 5. IPA suppresses PXR ubiquitination and anchors P65. (A, B) BMMs were infected with PXR-overexpressing lentivirus (over-PXR) or the GFP lentivirus (GFP) and then cultured in the presence of M-CSF and RANKL for 5 days. TRAP staining was performed, and TRAP-positive cells with three or more nuclei were counted as osteoclasts. (C, D) BMMs were seeded onto the Osteo Assay strip well plates and infected with lentivirus carrying Over-OXR or GFP and then cultured in the presence of M-CSF and RANKL for 5 days. F-actin staining was then performed, and three patterns of podosomes—podosome clusters, actin rings, and podosome belts—were counted. (E, F) BMMs were treated as described in (C, D); the cells were washed from the surface by using 10% bleaching solution for 5 min. Resorption pits were captured with a light microscopy and analyzed using Image J software. (G-J) BMMs were seeded onto six-well plates and infected with Over-PXR or GFP lentivirus and then cultured in the presence of M-CSF with or without stimulation of RANKL for 5 days. Relative mRNA expression of osteoclast-specific genes was quantified using qPCR. (K) BMMs were treated as described in (G-J). Protein expression of osteoclast-specific genes and PXR was determined using Western blotting. (L) Western blotting assay examined the activation of NF-kappa B signaling pathway after PXR over expression. (M) Protein levels of PXR after RANKL treatment were measured at indicated time points with or without IPA pretreatment. (P) BMMs were seeded on six-well plates and incubated with 30 ng/mL M-CSF and 75 ng/mL RANKL for 5 days; MG132 (10 μM) was added 4 hours before harvesting. Total-cell lysates were subjected to immunoprecipitation using anti-PXR antibody. Immunoprecipitates were separated by SDS-PAGE and immunoblotted using anti-ubiquitin antibody. (Q) BMMs were seeded on six-well plates and incubated with 30 ng/mL M-CSF and 75 ng/mL RANKL for 5 days. Total-cell lysates were subjected to immunoprecipitation using anti-PXR antibody. Immunoprecipitates were separated by SDS-PAGE and immunoblotted using anti-P65 antibody. (R) Representative immunofluorescence images showing P65 (green), PXR (red), and nucleus (blue) in cells incubated with 30 ng/mL M-CSF and 75 ng/mL RANKL with or without IPA (50 μM). * $P < 0.05$; ** $P < 0.01$; *** $P < 0.001$; NS, no significance.

3.7. C. spor. encapsulated SF hydrogel treatment inhibits OVX-induced bone loss

C. spor. colonization in combination with tryptophan supplementation in diet significantly protected against OVX-induced bone loss. However, the disadvantages of direct oral bacterial administration may prevent its translational use. First, live bacteria have to survive in the gastric fluid before colonizing the gut, which may disrupt stomach homeostasis. In addition, the relatively short gastrointestinal transit time in mice (approximately 8 h) [27] may limit sufficient *C. spor* colonization. To overcome these limitations, we developed an encapsulated SF hydrogel system for *C. spor.* delivery. Valentini L.'s study suggested silk fibroin films were stable in the simulated gastric fluid, however, can dissolve in the small and large intestines' neutral pH simulated intestine fluid [28]. In addition, a bioinformatic analysis suggested that silk fibroin is selectively degradable by enzymes in the small intestine, including chymotrypsin, but resilient to gastric pepsin [29].

The silk fibroin (SF) hydrogel was prepared via ultrasonic induction through the formation of a β-sheet structure and hydrogen bonds between intra- and intermolecular SF polymer chains. SEM images showed that the SF hydrogel possessed a honeycomb-like porous microstructure

(Fig. 7A). Enlarged images of the bacteria-encapsulated SF hydrogel (B@SF hydrogel) demonstrated even distribution of bacteria within the hydrogel network (Fig. 7A). The viscoelastic properties of the SF and B@SF hydrogels were investigated using rheological measurements. After sonication, the hydrogel was immediately subjected to a rheological sweep. As shown in Fig. 7B, the hydrogel's storage modulus (G') dramatically increased over time, attributed to the increased β-sheet crosslinking formation inside the hydrogel. Furthermore, the results of the time (Fig. 7B), frequency (Fig. 7C), and strain sweeps (Fig. 7D) showed no significant difference between the SF and B@SF hydrogel groups, demonstrating that bacterial encapsulation had no negative effect on hydrogel formation. To observe the distribution of the SF hydrogel in the gastrointestinal tract (GIT), an *in vivo* fluorescence imaging system and Cy5.5-conjugated SF were used. The imaging results showed that the fluorescence gradually moved from the anterior to the posterior GIT over time, and finally, the cecum and colorectum exhibited the strongest fluorescence intensity at 12 h (Fig. 7E). These results suggested that the B@SF hydrogel was effectively retained in the GIT and concentrated in the colorectal area in accordance with the peristaltic rhythm of the GIT. After 24 h of gavage, the fluorescence in the GIT showed a relatively low intensity, suggesting that the hydrogel was
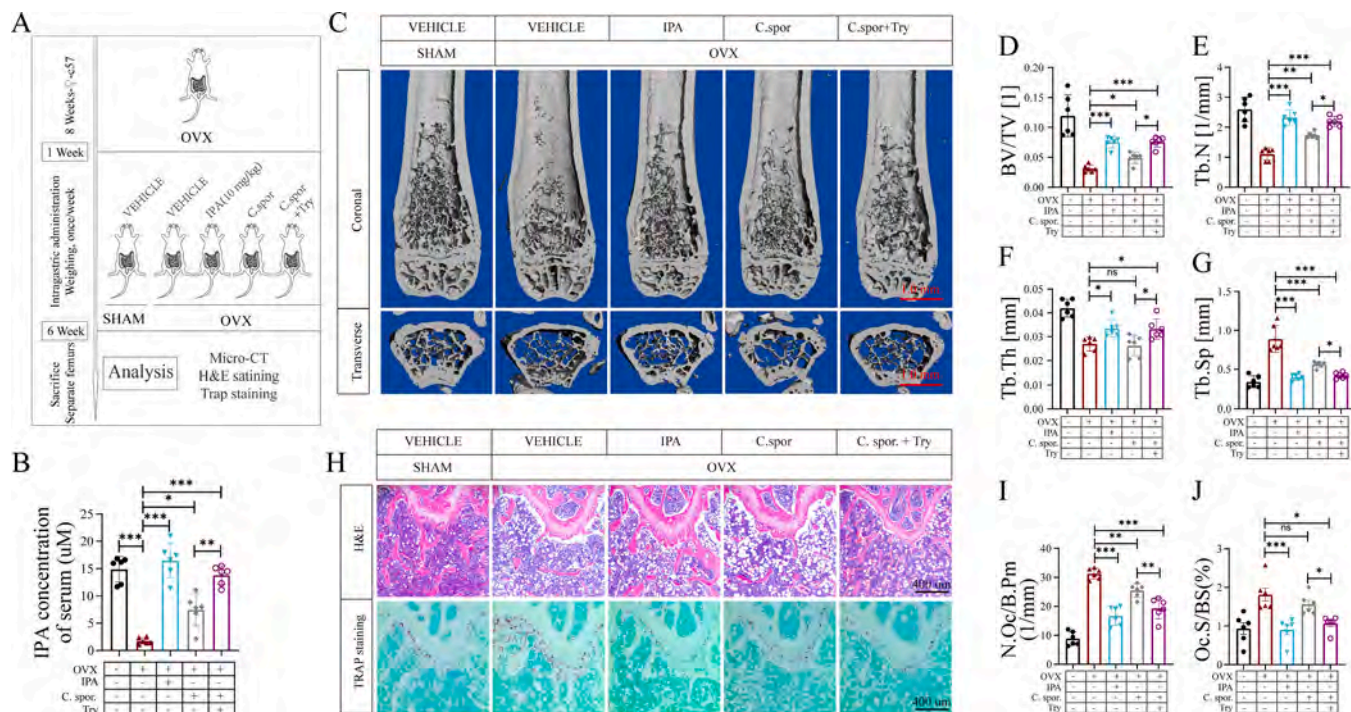
Fig. 6. Both IPA supplement and *C. spor.* colonization protect mice against OVX-induced bone loss. (A) Schematic diagram of the animal study. (B) Serum concentrations of IPA in each group. (C) Representative 3D-reconstructed images of the distal femurs of mice in each group. Red scale bar refers to 1.0 mm. (D-G) Quantitative analyses of bone structural parameters of the distal femurs, including bone volume/tissue volume (BV/TV), trabecular numbers (Tb.N), trabecular thickness (Tb.Th), and trabecular space (Tb.Sp). (H) Representative sections of the distal femurs visualized using H&E (scale bar = 1000 μm) and TRAP (scale bar = 1000 μm) staining. (I, J) Quantitative analyses of histomorphometric bone parameters, including N.Oc/B.Pm and Oc.S/BS, were performed. All data are presented as mean ± SEM. * P < 0.05; ** P < 0.01; *** P < 0.001; NS, no significance.
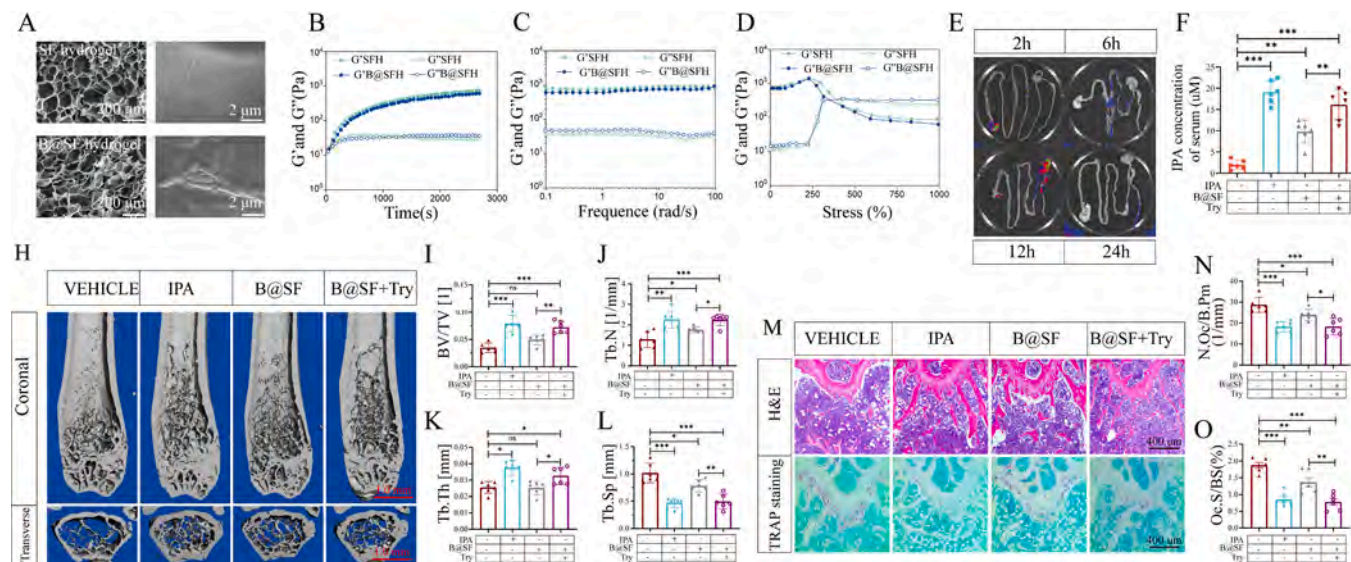
Fig. 7. *C. spor.*-encapsulated SF hydrogel treatment inhibits OVX-induced bone loss. (A) SEM of silk fibroin (SF) hydrogel and bacteria-encapsulated SF (B@SF) hydrogel. Results of time sweep (B), frequency sweep (C), and strain sweep (D) showed no difference between the SF and B@SF hydrogels. (E) *In vivo* intestinal retention effect of SF and B@SF hydrogels. (F) Serum concentrations of IPA in each group. (H) Representative 3D-reconstructed images of the distal femurs of mice in each group. Red scale bar refers to 1.0 mm. (I-L) Quantitative analyses of bone structural parameters of the distal femurs, including BV/TV, Tb.N, Tb.Th, and Tb.Sp. (M) Representative sections of the distal femurs visualized using H&E (scale bar = 1000 μm) and TRAP (scale bar = 1000 μm) staining. (N, O) Quantitative analyses of histomorphometric bone parameters, including N.Oc/B.Pm and Oc.S/BS, were performed. All data are presented as mean ± SEM. * P < 0.05; ** P < 0.01; *** P < 0.001; NS, no significance.

expelled from the body. These data suggest that the SF hydrogel is a suitable oral carrier for delivering bacteria to the GIT and prolonging their retention time in the GIT.

Further *in vivo* experiments showed that B@SF hydrogel administration five times at 3-day intervals significantly increased serum IPA levels (Fig. 7F). When the B@SF hydrogel was administered with

tryptophan supplementation, this effect was further enhanced. μCT scanning demonstrated that B@SF hydrogel administration alone partially prevented OVX-induced bone loss (Fig. 7H-L). Meanwhile, B@SF hydrogel administration with a tryptophan diet achieved comparable protection against OVX-induced bone loss to daily IPA supplementation, as revealed by increased BMD, BV/TV, Tb.N and decreased Tb.Sp (Figs. 7H-L and S10). Furthermore, H&E and TRAP staining of the bone sections indicated Oc.S/BS (%) (Fig. 7M-O). In addition, there was not difference in mice body weight, serum T-bil, CRE, UREA and activity of ALT and AST between control group and B@SF hydrogel group, which indicated the safety of B@SF hydrogel treatment (Fig. S10). Overall, *C. spor.*-encapsulated SF hydrogel treatment is a convenient, safe and effective method for combating OVX-induced bone loss.

4. Discussion

In this study, we investigated the contribution of gut microbiome to the pathogenesis of postmenopausal osteoporosis in a mouse model. The results identified *C. spor.*, as well as its derived metabolite IPA, to be decreased in OVX mice. IPA was found to suppress osteoclast differentiation *in vitro* by activating PXR, which led to increased binding of PXR with P65. Administering *C. spor.* in combination with tryptophan supplement diet provided similar protection against OVX-induced bone loss as direct IPA administration. To minimize repeated drug or microbiota administration, we developed the *C. spor.*-encapsulated SF hydrogel system, which offered comparable protection against OVX-induced bone loss with 5 interval times treatment compared with direct *C. spor.* colonization for 15 consecutive days or IPA gavage for 42 days. Although we checked the bone phenotype of mice with *C. spor.* colonization after 4 weeks of the last treatment, longer bone protection may be expected.

The changes of gut microbiota composition in postmenopausal women and its correlation with bone mass have been a matter of debate. Decreased gut *Clostridia* were identified in osteoporotic and osteopenic postmenopausal women compared to healthy controls [11], confirming the correlation of abundance of gut *Clostridia* and postmenopausal osteoporosis. However, another study performed in human subjects suggest that *Veillonella, Parabacteroides* and *Harryflintia* were mainly enriched in postmenopausal osteoporosis (PMO) group, while *Veillonella, Prevotella,* and *Enterobacterium* mainly appeared in healthy postmenopausal women [30]. In contrast, the abundances of *Lactobacillales, Coriobacteriales, Parabacteroides* and *Lactobacillus* were significantly higher in the PMO group than in the control group, whereas relative abundances of *Bacteroides massiliensis, Lachnospira pectinoschiza, Bacteroides coprocola* and *Blautia* were significantly higher in the control group than in the PMO group [12]. In a recent released study performed in mice, α-proteobacteria and Firmicutes were significantly increased but Bacteroidetes decrease in the OVX group compared to the SHAM group [31]. The inconsistency between these studies warrants further investigations due to the limited sample size. In addition, gut microbiota is affected by a complex combination of environmental and host factors. Further studies performed in multiple centers may clarify the debate.

It's worth noting that, other than *C. spor.*, *C. cadaveris, C. botulinum,* and *Peptostreptococcus anaerobius* have also been shown to produce IPA from tryptophan [32]. However, the relative contributions of different bacteria to IPA in circulation remain unknown. Our study here revealed IPA suppressed osteoclast formation, however, did not affect osteoblast differentiation *in vitro*. Meanwhile, previous study showed PXR-knockout mice exhibited decreased bone volume resulting from enhanced bone resorption and reduced bone formation [33]. The IPA-PXR interaction in osteoblasts may need further investigation to explain the controversy.

PXR has emerged as a promising target in energy homeostasis, immune responses, and cancer [34]. Rifampicin, a PXR agonist, was used in a phase 4 clinical trial to evaluate its effects on glucose, lipid, and hormone homeostasis [35] [36] [37]. These results indicate that PXR is

a safe treatment target in humans and may be promising for combating bone diseases. However, rifampicin is widely used as anti-mycobacteria drug in clinic. There are some concerns of increased rifampicin resistancy in clinic, which may affect the efficiency of this drug in anti-mycobacteria [38]. Instead, *C. spor.* colonization may be a promising replacement in these cases.

Microbiota transplantation has been used clinically to treat recurrent *C. difficile* infections. However, the delivery routes for microbiota transplantation are associated with adverse events, with transplantation via the upper GIT having higher incidence rates of adverse events (43.9%) than that via the lower gastrointestinal tract (20.6%) [39]. After oral administration, the microbiota pass through the GIT from the mouth and stomach to the small intestine and colon. In the stomach, the microbiota are exposed to acidic gastric fluid, which is lethal to most bacteria. In addition, the viability of transplanted microbiota is affected by ionic strength, pepsin activity, and mechanical churning [40]. Methods such as enteric coating and enteric microencapsulated formulations have been developed to protect probiotics against the harsh environment in the stomach and help probiotic bacteria colonize the intestine or colon [41]. The SF hydrogel system reported here delays gastrointestinal transit time, allowing for colonization of more bacteria in the gut and improved survival of loaded bacteria in the harsh stomach environment. Meanwhile, the additional increase of femur bone mass in the *C. spor.* colonization group with tryptophan enriched diet compared with *C. spor.* colonization alone group highlights the benefits of tryptophan supplement. Fortunately, food enriched in tryptophan such as red meat, soybeans, fish, cheese is easily accessible [42].

In conclusion, this study identified that *C. spor.* in the gut and its derived IPA were decreased in OVX mice. Administration of the *C. spor.*-encapsulated SF hydrogel system protected OVX mice from bone loss, thus offering a promising treatment method for postmenopausal osteoporosis.

Author contributions

LF and PRP conceived of and designed the study. PRP and SC performed most of the experiments, analyzed the data, and wrote the manuscript. LF, GHF, and FQ provided guidance and advice during the experimentation and analysis of the results. LHY, KHL, DYM, and XY assisted with animal experiments. GSQ and FQ provided the essential reagents, equipment, and advice. LF and GHF provided feedback on the experiments and reviewed and edited the manuscript. Final approval of the manuscript was obtained from all the authors. All authors contributed to the manuscript and approved the submitted version.

CRediT authorship contribution statement

Hanfeng Guan: Resources, Supervision. **Shuangquan Gou:** Data curation, Formal analysis, Investigation, Validation. **Qian Feng:** Resources, Supervision, Validation. **Chao Song:** Investigation, Methodology, Validation, Writing – original draft, Writing – review & editing. **Feng Li:** Conceptualization, Funding acquisition, Investigation, Supervision, Writing – original draft. **Honglei Kang:** Methodology, Validation. **Haiyang Liu:** Investigation. **Yimin Dong:** Formal analysis, Methodology. **Yong Xu:** Investigation, Methodology. **Kaiyong Cai:** Supervision, Visualization. **Renpeng Peng:** Conceptualization, Data curation, Investigation, Writing – original draft. **Peixuan Hu:** Data curation, Formal analysis, Resources, Software.

Declaration of Competing Interest

The authors declare no competing interests.

Data availability

Data will be made available on request.

Acknowledgments

Appendix A. Supporting information

Supplementary data associated with this article can be found in the online version at doi:10.1016/j.phrs.2024.107121.

References

[1] A. Duran, M. Serrano, M. Leitges, J.M. Flores, S. Picard, J.P. Brown, J. Moscat, M. T. Diaz-Meco, The atypical PKC-interacting protein p62 is an important mediator of RANK-activated osteoclastogenesis, Dev. Cell 6 (2) (2004) 303–309.

[2] J. Mizukami, G. Takaesu, H. Akatsuka, H. Sakurai, J. Ninomiya-Tsuji, K. Matsumoto, N. Sakurai, Receptor activator of NF-kappaB ligand (RANKL) activates TAK1 mitogen-activated protein kinase kinase kinase through a signaling complex containing RANK, TAB2, and TRAF6, Mol. Cell. Biol. 22 (4) (2002) 992–1000.

[3] Y. Abu-Amer, NF-kappaB signaling and bone resorption, Osteoporos. Int. 24 (9) (2013) 2377–2386.

[4] K. Lee, I. Seo, M.H. Choi, D. Jeong, Roles of mitogen-activated protein kinases in osteoclast biology, Int. J. Mol. Sci. 19 (10) (2018).

[5] K. Sjogren, C. Engdahl, P. Henning, U.H. Lerner, V. Tremaroli, M.K. Lagerquist, F. Backhed, C. Ohlsson, The gut microbiota regulates bone mass in mice, J. Bone Miner. Res. Off. J. Am. Soc. Bone Miner. Res. 27 (6) (2012) 1357–1367.

[6] J. Yan, J.W. Herzog, K. Tsang, C.A. Brennan, M.A. Bower, W.S. Garrett, B.R. Sartor, A.O. Aliprantis, J.F. Charles, Gut microbiota induce IGF-1 and promote bone formation and growth, Proc. Natl. Acad. Sci. USA 113 (47) (2016) E7554–E7563.

[7] S.W. Cho, J.H. An, H. Park, J.Y. Yang, H.J. Choi, S.W. Kim, Y.J. Park, S.Y. Kim, M. Yim, W.Y. Baek, J.E. Kim, C.S. Shin, Positive regulation of osteogenesis by bile acid through FXR, J. Bone Miner. Res. Off. J. Am. Soc. Bone Miner. Res. 28 (10) (2013) 2109–2121.

[8] M. Go, E. Shin, S.Y. Jang, M. Nam, G.S. Hwang, S.Y. Lee, BCAT1 promotes osteoclast maturation by regulating branched-chain amino acid metabolism, Exp. Mol. Med. 54 (6) (2022) 825–833.

[9] Y. Su, A. Elshorbagy, C. Turner, H. Refsum, R. Chan, T. Kwok, Circulating amino acids are associated with bone mineral density decline and ten-year major osteoporotic fracture risk in older community-dwelling adults, Bone 129 (2019) 115082.

[10] N. Wang, Y. Hao, L. Fu, Trimethylamine-N-oxide promotes osteoclast differentiation and bone loss via activating ROS-dependent NF-kappaB signaling pathway, Nutrients 14 (19) (2022).

[11] E.A. Rettedal, B.L. Ilesanmi-Oyelere, N.C. Roy, J. Coad, M.C. Kruger, The gut microbiome is altered in postmenopausal women with osteoporosis and osteopenia, JBMR 5 (3) (2021) e10452.

[12] J. He, S. Xu, B. Zhang, C. Xiao, Z. Chen, F. Si, J. Fu, X. Lin, G. Zheng, G. Yu, J. Chen, Gut microbiota and metabolite alterations associated with reduced bone mineral density or bone metabolic indexes in postmenopausal osteoporosis, Aging 12 (9) (2020) 8583–8604.

[13] Y.W. Zhang, M.M. Cao, Y.J. Li, P.P. Lu, G.C. Dai, M. Zhang, H. Wang, Y.F. Rui, Fecal microbiota transplantation ameliorates bone loss in mice with ovariectomy-induced osteoporosis via modulating gut microbiota and metabolic function, J. Orthop. Transl. 37 (2022) 46–60.

[14] B. Shin, J. Kupferman, E. Schmidt, F. Polleux, A.M. Delany, S.K. Lee, Rac1 inhibition via Srgap2 restrains inflammatory osteoclastogenesis and limits the clastokine, SLIT3, J. Bone Miner. Res. 35 (4) (2020) 789–800.

[15] Q. Guo, H. Kang, J. Wang, Y. Dong, R. Peng, H. Zhao, W. Wu, H. Guan, F. Li, Inhibition of ACLY leads to suppression of osteoclast differentiation and function via regulation of histone acetylation, J. Bone Miner. Res. (2021).

[16] Z. Li, X. Yang, R. Fu, Z. Wu, S. Xu, J. Jiao, M. Qian, L. Zhang, C. Wu, T. Xie, J. Yao, Z. Wu, W. Li, G. Ma, Y. Chen, H.K. Zhang, Y. Cheng, X. Tang, P. Wu, G. Lian, H. Wei, J. Zhao, J. Xu, L. Ai, S. Siwko, Y. Wang, J. Ding, G. Song, J. Luo, M. Liu, J. Xiao, Kisspeptin-10 binding to Gpr54 in osteoclasts prevents bone loss by activating Dusp18-mediated dephosphorylation of Src, Nat. Commun. 15 (1) (2024) 1300.

[17] Y. Xiong, S. Liu, H. Xiao, Q. Wu, L. Chi, L. Zhu, L. Fang, Y. Li, Z. Jiang, L. Wang, Dietary stevia residue extract supplementation improves the performance and antioxidative capacity of growing-finishing pigs, J. Sci. Food Agric. 102 (11) (2022) 4724–4735.

[18] H.M. Roager, T.R. Licht, Microbial tryptophan catabolites in health and disease, Nat. Commun. 9 (1) (2018) 3294.

[19] M. Michalowska, B. Znorko, T. Kaminski, E. Oksztulska-Kolanek, D. Pawlak, New insights into tryptophan and its metabolites in the regulation of bone metabolism, J. Physiol. Pharmacol. 66 (6) (2015) 779–791.

[20] V. Fischer, M. Haffner-Luntzer, Interaction between bone and immune cells: implications for postmenopausal osteoporosis, Semin. Cell Dev. Biol. 123 (2022) 14–21.

[21] W.S.S. William, J. Boyle, David L. Lacey, Osteoclast differentiation and activation, Nature 423 (2003) 337–342.

[22] Z. Sari, E. Miko, T. Kovacs, L. Janko, T. Csonka, G. Lente, E. Sebo, J. Toth, D. Toth, P. Arkosy, A. Boratko, G. Ujlaki, M. Torok, I. Kovacs, J. Szabo, B. Kiss, G. Mehes, J. J. Goedert, P. Bai, Indolepropionic acid, a metabolite of the microbiome, has cytostatic properties in breast cancer by activating AHR and PXR receptors and inducing oxidative stress, Cancers 12 (9) (2020).

[23] H.W. Xiao, M. Cui, Y. Li, J.L. Dong, S.Q. Zhang, C.C. Zhu, M. Jiang, T. Zhu, B. Wang, H.C. Wang, S.J. Fan, Gut microbiota-derived indole 3-propionic acid protects against radiation toxicity via retaining acyl-CoA-binding protein, Microbiome 8 (1) (2020) 69.

[24] R. Rana, S. Coulter, H. Kinyamu, J.A. Goldstein, RBCK1, an E3 ubiquitin ligase, interacts with and ubiquinates the human pregnane X receptor, Drug Metab. Dispos. 41 (2) (2013) 398–405.

[25] X. Gu, S. Ke, D. Liu, T. Sheng, P.E. Thomas, A.B. Rabson, M.A. Gallo, W. Xie, Y. Tian, Role of NF-kappaB in regulation of PXR-mediated gene expression: a mechanism for the suppression of cytochrome P-450 3A4 by proinflammatory agents, J. Biol. Chem. 281 (26) (2006) 17882–17889.

[26] J.Y. Li, H. Tawfeek, B. Bedi, X. Yang, J. Adams, K.Y. Gao, M. Zayzafoon, M. N. Weitzmann, R. Pacifici, Ovariectomy disregulates osteoblast and osteoclast formation through the T-cell receptor CD40 ligand, Proc. Natl. Acad. Sci. USA 108 (2) (2011) 768–773.

[27] P. Padmanabhan, J. Grosse, A.B. Asad, G.K. Radda, X. Golay, Gastrointestinal transit measurements in mice with 99mTc-DTPA-labeled activated charcoal using NanoSPECT-CT, EJNMMI Res. 3 (1) (2013) 60.

[28] L. Valentini, L. Pacini, F. Errante, C. Morchio, B. Sanna, P. Rovero, A. Morabito, Peptide-functionalized silk fibers as a platform to stabilize gelatin for use in ingestible devices, Molecules 27 (14) (2022).

[29] N. Navamajiti, A. Gardner, R. Cao, Y. Sugimoto, J.W. Yang, A. Lopes, N.V. Phan, J. Collins, T. Hua, S. Damrongsakkul, S. Kanokpanont, C. Steiger, D. Reker, R. Langer, G. Traverso, Silk fibroin-based coatings for pancreatin-dependent drug delivery, J. Pharm. Sci. 113 (3) (2024) 718–724.

[30] H. Wang, J. Liu, Z. Wu, Y. Zhao, M. Cao, B. Shi, B. Chen, N. Chen, H. Guo, N. Li, J. Chen, R. Xu, Gut microbiota signatures and fecal metabolites in postmenopausal women with osteoporosis, Gut Pathog. 15 (1) (2023) 33.

[31] Z. Guan, Z. Xuanqi, J. Zhu, W. Yuan, J. Jia, C. Zhang, T. Sun, H. Leng, C. Jiang, Y. Xu, C. Song, Estrogen deficiency induces bone loss through the gut microbiota, Pharmacol. Res. 196 (2023) 106930.

[32] D. Dodd, M.H. Spitzer, W. Van Treuren, B.D. Merrill, A.J. Hryckowian, S. K. Higginbottom, A. Le, T.M. Cowan, G.P. Nolan, M.A. Fischbach, J.L. Sonnenburg, A gut bacterial pathway metabolizes aromatic amino acids into nine circulating metabolites, Nature 551 (7682) (2017) 648–652.

[33] K. Azuma, S.C. Casey, M. Ito, T. Urano, K. Horie, Y. Ouchi, S. Kirchner, B. Blumberg, S. Inoue, Pregnane X receptor knockout mice display osteopenia with reduced bone formation and enhanced bone resorption, J. Endocrinol. 207 (3) (2010) 257–263.

[34] C. Lynch, S. Sakamuru, R. Huang, J. Niebler, S.S. Ferguson, M. Xia, Characterization of human pregnane X receptor activators identified from a screening of the Tox21 compound library, Biochem. Pharmacol. 184 (2021) 114368.

[35] F. Hassani-Nezhad-Gashti, J. Rysa, O. Kummu, J. Napankangas, M. Buler, M. Karpale, J. Hukkanen, J. Hakkola, Activation of nuclear receptor PXR impairs glucose tolerance and dysregulates GLUT2 expression and subcellular localization in liver, Biochem. Pharmacol. 148 (2018) 253–264.

[36] F. Hassani-Nezhad-Gashti, T. Salonurmi, H. Hautajarvi, J. Rysa, J. Hakkola, J. Hukkanen, Pregnane X receptor activator rifampin increases blood pressure and stimulates plasma renin activity, Clin. Pharmacol. Ther. 108 (4) (2020) 856–865.

[37] R. Rahunen, O. Kummu, V. Koivukangas, H. Hautajarvi, J. Hakkola, J. Rysa, J. Hukkanen, Pregnane X receptor4beta-hydroxycholesterol axis in the regulation of overweight- and obesity-induced hypertension, J. Am. Heart Assoc. 11 (6) (2022) e023492.

[38] B.P. Goldstein, Resistance to rifampicin: a review, J. Antibiot. 67 (9) (2014) 625–630.

[39] S. Bonovas, G. Fiorino, T. Lytras, G. Nikolopoulos, L. Peyrin-Biroulet, S. Danese, Systematic review with meta-analysis: use of 5-aminosalicylates and risk of colorectal neoplasia in patients with inflammatory bowel disease, Aliment. Pharmacol. Ther. 45 (9) (2017) 1179–1192.

[40] L.K. Sarao, M. Arora, Probiotics, prebiotics, and microencapsulation: a review, Crit. Rev. Food Sci. Nutr. 57 (2) (2017) 344–371.

[41] C. Yus, R. Gracia, A. Larrea, V. Andreu, S. Irusta, V. Sebastian, G. Mendoza, M. Arruebo, Targeted release of probiotics from enteric microparticulated formulations, Polymers 11 (10) (2019).

[42] F.M. Zuraikat, R.A. Wood, R. Barragan, M.P. St-Onge, Sleep and diet: mounting evidence of a cyclical relationship, Annu. Rev. Nutr. 41 (2021) 309–332.